Journal of CO2 Utilization 97 (2025) 103138

Contents lists available at ScienceDirect

Journal of CO2 Utilization

journal homepage: www.elsevier.com/locate/jcou

# Investigation of the performance and stability of copper and brass nanoparticles for $CO_2$ reduction in organic electrolytes

Ruth Witzel [a], Leonie Wildersinn [a], Enrico Tusini [b,c], Steffen Czioska [b], Inga Dorner [a], Anna Zimina [c], Jan-Dierk Grunwaldt [b,c], Philipp Röse [a,*]

[a] Institute for Applied Materials – Electrochemical Technologies, Karlsruhe Institute of Technology, Adenauerring 20b, Karlsruhe 76131, Germany
[b] Institute for Chemical Technology and Polymer Chemistry, Karlsruhe Institute of Technology, Engesserstraße 20, Karlsruhe 76131, Germany
[c] Institute of Catalysis Research and Technology, Karlsruhe Institute of Technology, Hermann-von-Helmholtz-Platz 1, Eggenstein-Leopoldshafen 76344, Germany

ARTICLE INFO

*Keywords:*
$CO_2$RR
CuZn catalyst
Nanoparticles
Electrocatalysis
Organic electrolyte

ABSTRACT

Numerous catalysts and reaction conditions with improved performance, selectivity, and stability for the electrochemical $CO_2$ reduction reaction have been reported. However, little is known about the influence of binary catalysts and their role on this reaction in organic electrolytes. Thus, we herein report on the catalyst characteristics of copper and copper-zinc nanoparticles for $CO_2$ reduction in aprotic electrolytes. We provide insights into the impact of varying CuZn ratios on the performance and stability, showing that brass in the α-phase has lower overpotentials and a higher electrochemical activity, with an optimum for CuZn 80/20. Although using the same catalyst, we compared acetonitrile and *N*,*N*-dimethylformamide based electrolytes, and found the highest performance for acetonitrile. Under anhydrous conditions, absolute control of Faradaic efficiency is possible, resulting in > 95 % CO; only traces of oxalate and no parasitic hydrogen evolution were found. Our study reveals that aside from proper process conditions for $CO_2$ reduction in organic electrolytes, the design of the catalysts plays an equally decisive role for improved performance, selectivity and stability.

## 1. Introduction

The electrocatalytic $CO_2$ reduction on Cu-based catalysts is a promising approach to close the carbon cycle and create a carbon-neutral energy scheme in which $CO_2$ is reduced electrochemically to produce valuable chemicals[1]. As the kinetics of electrochemical $CO_2$ reduction are sluggish, well-defined catalyst materials and process conditions are required to reduce the energy demand of the process and, at the same time, enable high selectivity towards the valuable products and long-term stability[2]. Numerous research efforts have been made to identify the best combination of Cu-based catalyst material, electrolyte composition, and process conditions for high reaction rates and selectivity[3–6]. However, challenges in selectivity control toward $C_{2+}$ products in aqueous electrolytes remain unsolved[7,8]. As aqueous electrolytes have been widely studied due to their ease of use, low cost and environmental safety[9,10], the balance of $CO_2$ and proton concentrations are challenging. Their use leads to multiple limitations, including: surface changes between metallic copper and its oxides [11–15], a large product variety[10,16,17], the low $CO_2$ solubility which leads to $CO_2$ mass transport limitations[16,18], the consumption of $CO_2$ by the carbonate equilibrium [19] as well as the competing hydrogen evolution reaction (HER)[20,21].

To overcome well-known challenges in aqueous electrolytes, aprotic organic electrolytes have been a viable alternative[22,23], as they have five times higher $CO_2$ solubility (e.g., MeCN = 0.314 mol $L^{-1}$, DMF = 0.194 mol $L^{-1}$, $H_2O$ = 0.0345 mol $L^{-1}$)[24,25]. The use of organic solvents lead to a proton free environment [26], and the higher $CO_2$ solubility also mitigates transport limitations that typically occur in aqueous electrolytes[27]. However, using organic electrolytes comes with other challenges, such as higher overpotentials. Highly active electrocatalysts are needed to reduce overpotentials and accelerate kinetics[28]. The main focus studying aprotic organic electrolytes has been on experimental studies[29–37], and a few model-based analyses on microkinetics[8,38–40], as well as process studies[40,41]. A fundamental understanding of the reaction mechanism in these environments is thus essential to guide catalyst design.

Mechanistically, $CO_2$ reduction in aprotic organic electrolytes differs from aqueous electrolytes, as it mainly yields in CO, carbonate, and

* Corresponding author.
*E-mail address:* philipp.roese@kit.edu (P. Röse).

https://doi.org/10.1016/j.jcou.2025.103138
Received 28 February 2025; Received in revised form 11 May 2025; Accepted 25 May 2025
Available online 28 May 2025

oxalate when no additional proton source is available[42], leading to high selectivity control. Traces of $H_2$ and formate are found in experiments from protons from residual water. This is due to a difference in the reaction mechanism for $CO_2$RR, as proposed first in the 80 s by Amatore and Savéant (Fig. 1)[22,31].

First, $CO_2$ from the electrolyte adsorbs onto free sites on the electrode surface and undergoes a reductive one-electron transfer. This results in the formation of an adsorbed $*CO_2^{\bullet-}$, which requires high overpotentials and, thus, considered the rate-determining step[22]. However, our recent work on kinetic modeling of reaction and transport processes in $CO_2$ reduction on Cu catalyst surfaces in organic electrolytes showed that $CO_2$ adsorption is rate-limiting[38]. After the formation of the $*CO_2^{\bullet-}$, two potential pathways, either towards CO or oxalate, can follow. The selectivity towards the two products is still not fully clarified but thought to depend on the binding affinity of $*CO_2/*CO_2^{\bullet-}$ on the catalyst surface and the stabilization of the $CO_2^{\bullet-}$ in the electrolyte[42,43]. If the binding affinity is sufficiently high, such as for Cu or Ag, the $*CO_2^{\bullet-}$ reacts with a second $CO_2$ to a carbonic formic anhydride and undergoes an electrochemically coupled disproportionation reaction to form CO and carbonate as product (pathway A)[44,45]. When catalysts with weak or no interactions are used as electrode material, such as Hg or Pb, the $*CO_2^{\bullet-}$ intermediate can also desorb from the catalyst surface and dimerize with a second desorbed $CO_2^{\bullet-}$ in the electrolyte to form oxalate (pathway B).

For metallic Cu as catalyst material in acetonitrile, selectivities of $>$ 75 % towards CO and no oxalate formation were shown by Ikeda *et al.* and Deacon-Price *et al.* [31,46], these findings were supported by in situ RAMAN and FTIR experiments [47]. Bagger and coworkers developed a microkinetic model for $CO_2$RR using rates estimated from density functional theory (DFT) to predict the selectivities of various transition metal catalysts. Their proposed mechanism provides insights into the CO pathway, in which a single adsorbed $*CO_2$ and a second $CO_2$ from the solution react with each other rather than two neighboring adsorbed $*CO_2$ and $*CO_2^{\bullet-}$ [8].

The choice of catalyst material remains a critical factor in determining both selectivity and stability. While alloying strategies have been extensively explored in aqueous electrolytes to tailor the electronic structure and modulate the binding strength of key intermediates [48–50], their application in aprotic electrolytes remains unexplored. At the same time, the influence of the electrolyte must not be overlooked, as it directly affects product distribution. Commonly used aprotic polar solvents include *N,N*-dimethylformamide (DMF)[23], acetonitrile (MeCN)[32,47,51], dimethyl sulfoxide (DMSO)[52], and propylene carbonate[53] each offering distinct physicochemical properties that can impact activity and selectivity.

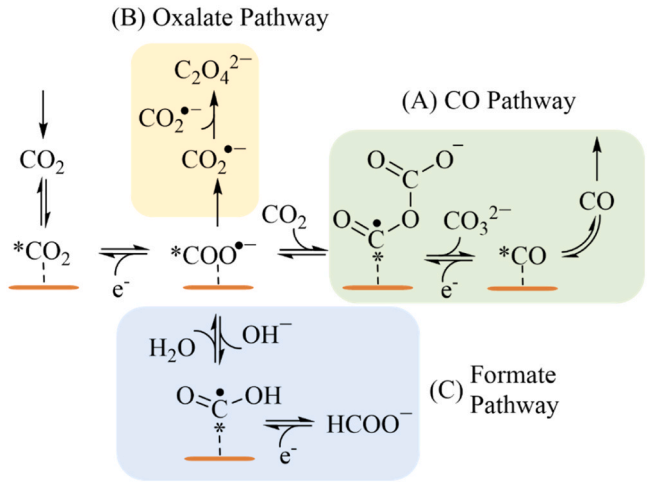


**Fig. 1.** Reaction mechanism of the electrochemical $CO_2$ reduction in organic electrolytes on a copper electrode: (A) towards carbon monoxide and carbonate (B) towards oxalate (C) towards formate with residual amounts of water in the system. Asterix (*) denotes the active Cu center and adsorbed species.

Only a few studies have investigated the effect of the solvents beyond electrochemical activity. The characteristics of the electrolyte used have been found to influence the product selectivity; it was shown that a low electrolyte nucleophilicity and a high $CO_2$ diffusion coefficient lead to a higher FE towards CO with MeCN-containing electrolytes than with DMF[54]. In addition, the quaternary ammonium salts used to improve ionic conductivity can stabilize the $CO_2^{\bullet-}$, leading to increased oxalate formation[55]. Decreasing length of the alkyl chain of the tetraalkylammonium salt and decreasing cation size leads to an increase in CO formation rates in aprotic media[56]. This highlights the importance of considering both the catalyst and electrolyte as determining factors for $CO_2$RR performance and selectivity.

Despite the extensive use of Cu and bimetallic catalysts such as CuZn materials for $CO_2$RR in aqueous processes – owing to their low cost, abundance, and wide product distribution – their applicability and behavior in aprotic organic electrolytes remains unsolved. In particular, little is known about how alloy composition influences catalytic activity, selectivity and long-term structural stability under non-aqueous conditions. In this study, we systematically investigate Cu and CuZn nanoparticles with varying Zn content, focusing on their morphology, electrochemical performance, and bulk stability in aprotic electrolytes. We demonstrate that incorporating small amounts of Zn into Cu significantly enhances the electrochemical activity, without altering the product distribution. Unlike in aqueous processes, the oxidation state of the catalyst remains largely unchanged over extended electrolysis, indicating high bulk stability under aprotic conditions. Our findings demonstrate the viability of CuZn catalysts in organic electrolytes and highlight the potential of aprotic electrolytes for efficient and stable $CO_2$ reduction.

## 2. Experimental section

### 2.1. Chemical and materials

$KHCO_3$ ($\geq$99.5 %), isopropanol (99.5 %), formic acid (98–100 %) and ethanol (99.8 %), NaOH (50 % in $H_2O$), $H_2SO_4$ (98 % in $H_2O$), acetic acid (96 %), Cu(II)acetate (98 %), Zn(II)acetate (99.9 %), methanol, ethylhexanoicacid (99 %), caproic acid (98 %) and $Cu_2O$ were purchased from Sigma-Aldrich. Isopropanol is distilled before use. Oxalic acid (98 %) was purchased from Roth. *N,N*-Dimethylformamide (DMF) ($\geq$99.5 %), Acetonitrile (MeCN) ($\geq$99.5 %), and Nafion® 5 % dispersion (D-520) were purchased from VWR. Solutions were, if not stated otherwise, used with the purity purchased. Tetra-*N*-butylammonium tetrafluoroborate ($TBABF_4$) (98 %) was purchased from abcr GmbH. CuO was purchased from Fluka. $CO_2$ ($\geq$99.995 %), Helium ($\geq$99.995 %), $N_2$ ($\geq$99.995 %), and CO ($\geq$99.995 %) were purchased from Air Liquide Germany GmbH. All aqueous solutions were prepared using ultrapure water (16 MΩ). The electrode carbon support material used was Freudenberg H23C2 and a glassy carbon rotating disc electrode (RDE, Pine research). For cleaning, polishing agent (5 μm and 0.3 μm aluminum oxide) purchased from (ALLIED-hightech) and polishing pads (Silicon carbide paper, adhesive back disc 2–7/8", 600 (P-1200) grit, ALLIED-hightech) were used.

### 2.2. Material characterization

X-ray diffraction (XRD) was performed using the Bruker D8 ADVANCE X-ray diffractometer using Cu K$\alpha$ radiation ($\lambda$= 1.54 Å) generated by accelerating electrons over 40 kV at an anode current of 40 mA. The intensity of the scattered X-rays was measured in a 2$\theta$-range of 20–100° with step sizes of 0.01° and 2 steps/s for qualitative analysis by Rietveld refinement (Software TOPAS). A full description of Rietveld refinement can be found in the Supporting Information.

The catalysts' morphology and crystalline structure were measured

using a scanning electron microscope (SEM, Supra 55VP, ZEISS FEG-SEM) with a field emission electron gun (FEG). The sizes of the recorded structures were evaluated using the program ImageJ 1.46. Conclusions about the sample's elemental composition could be drawn with the integrated Oxford Instrument energy-dispersive X-ray (EDX) spectrometer.

A complete trace element analysis was performed to obtain information about the composition of the different CuZnO-Nanoparticles (NP) after FSP. The analysis was performed with the iCAP™ RQ ICP-MS from Thermo Scientific™. For sample preparation, 25 mg CuZn NP were dissolved in 500 µl conc. $HNO_3$ and transferred into a 25 mL volumetric flask. It was filled up to the calibration mark with deionized water. To avoid small impurities, the liquid was filtered through a syringe filter. A blank sample was also prepared for the test measurement as described above but without adding the NP.

Karl-Fischer-Titration was performed by HHAC Labor Dr. Heusler GmbH. The titrant used was Hydranal® Composite 5 K, and the solvent was Hydranal® solvent. The extraction time was 0 s, and the measurement stop was at a 40 µL $min^{-1}$ drift.

### 2.3. Synthesis of CuO, ZnO, and CuZnO nanoparticle precursors

The CuO and ZnO nanoparticles were synthesized by flame spray pyrolysis (FSP), which has been used for the preparation of nanomaterials and catalysts[57,58], but rarely for electrocatalysts[59]. For the monometallic oxide catalysts, the copper salt precursor Cu(II)acetate (2 g) and zinc salt precursor Zn(II)acetate (2 g) were dissolved in a mixture of 100 mL MeOH and ethylhexanoicacid (1:1 v:v) to yield a final Cu concentration of 110.1 mM and Zn concentration of 109.0 mM. The solution was then placed into an ultrasonic sound bath for 1 h to ensure complete dissolution of the precursors. Subsequently, the resulting solution was filled into a 50 mL syringe and set into a syringe pump (Legato 210, KD Scientific Inc.). The solution was inserted with a flow rate of 5 mL $min^{-1}$ and dispersed with 5 NL $min^{-1}$ oxygen gas flow at 3 bar back pressure while it was released through a steel capillary of 0.413 mm diameter (Hamilton syringes, KF6, gauge 22). A supporting flame of 0.75 NL $min^{-1}$ methane and 1.6 NL $min^{-1}$ oxygen flow was used to enflame the dispersed solution. The synthesized NPs were collected in a cylindrical filter holder 80 cm over the flame by a glass fiber filter (Whatman GF6, GE) connected with a vacuum pump (R5, Busch). For the CuZnO mixed metal oxides, the Cu and Zn precursor ratios were adjusted to weight ratios of 80/20, 75/25, 50/50, and 25/75. The prepared solution was then treated and sprayed in the same manner as the single metal salt solution.

### 2.4. Electrochemical measurements

Electrochemical measurements were conducted using a RDE setup (PINE Research Instrumentation Inc.) with a glassy carbon electrode (A = 0.1963 $cm^2$) coated with metal oxide. The setup was connected to a potentiostat/galvanostat (Interface 1010E, Gamry). A glass cell (125 mL) was equipped with the RDE as a working electrode, a Pt wire as a counter electrode that was separated by a glass tube with a glass frit, and a reference electrode. In aqueous electrolytes, a reversible hydrogen electrode (RHE, stored in $H_2O$) was used; in organic electrolytes, the Ag/AgCl ($KCl_{sat}$ in $H_2O$) reference electrode was used.

### 2.5. Electrode preparation

Catalyst ink was prepared by mixing 2 mg metal oxide, 250 µL isopropanol, 750 µL deionized water, 8.58 µL Nafion® 5 % dispersion, and 1.2 µL of 1 M NaOH. The dispersions were ultrasonicated for 10 min. We previously reported this recipe for OER catalyst preparation[60]. For the rotating ring electrode experiment, the glassy carbon electrode was coated by dropping 10 µL of catalyst ink on the glassy carbon surface. The electrode was rotated at 100 rpm for 30 min to achieve a homogeneous coating. For the XRD analysis, Freudenberg H23C2 was coated using a brush until a loading of 2 g $cm^{-2}$ was reached. For product analysis, Freudenberg H23C2 electrodes with a geometric area of 4 $cm^2$ were coated with dry air using an airbrush. The coating was applied until a loading of 0.5 mg $cm^{-2}$ was reached.

Catalyst reduction of copper nanoparticles was performed in a 1 M NaOH (in $H_2O$) solution. The electrolyte was saturated with nitrogen for 15 minutes before the reduction procedure. Three cycles of CVs were conducted in a potential range of 1.5 V to −1.5 V vs. RHE. Afterward, CVs in a potential range of −0.3 V to −1.5 V were done; for the RDE measurements, 15 cycles; for the larger electrodes for product analysis, 50 cycles; and for the XRD samples, 150 cycles were carried out. All CVs were recorded with a scan rate of 100 mV $s^{-1}$. Reduction of CuZn nanoparticles was performed in 0.1 M $KHCO_3$ (in $H_2O$). The electrolyte was saturated with $N_2$ for 15 minutes before starting the reduction procedure. Three CV cycles were conducted in a potential range of 1 V to −1 V vs. RHE, and afterward, CVs in a potential range between −0.3 V and −1.3 V were done. Afterward, CVs in a potential range of −0.3 V to −1.5 V were used; for the RDE measurements, 15 cycles; for the electrodes for product analysis, 50 cycles; and for the XRD samples, 150 cycles were carried out. All CVs were done with a scan rate of 100 mV $s^{-1}$.

### 2.6. Electrochemical analyses

Cyclic voltammetry and chronoamperometry were used to analyze the electrochemical processes and for Tafel analysis. Potentials were *iR* corrected with bulk resistance $R_u$ determined by potentiostatic electrochemical impedance spectroscopy (EIS) after pre-conditioning at $E_{DC} = -0.8$ V in the high-frequency region from $10^6$ to $10^5$ Hz at a phase angle of $\varphi = 0°$; the amplitude was set to $\Delta E_{AC} = 10$ $mV_{rms}$. Electrolytes used were 0.1 M $TBABF_4$ in DMF and 0.1 M $TBABF_4$ in MeCN. The electrolyte was flushed with $CO_2$ for 20 min before each experiment, and the atmosphere above the electrolyte was continuously flushing with $CO_2$ during the entire experiment.

For each scan rate, five cycles of CVs were performed in a potential range of −0.8 V to −2 V vs. Ag/AgCl. Scan rates of 100 mV $s^{-1}$ and 50 mV $s^{-1}$ were used. CA measurements proceeded from −0.8 V to −2 V vs. Ag/AgCl in increments of 0.05 V and reverse. Each potential was held for 300 s.

### 2.7. Determination of the electrochemically active surface area

Electrochemically active surface area (ECSA) was determined by double-layer capacitance ($C_{DL}$) measurements performed in aqueous 0.1 M $KHCO_3$ solution. To determine the potential range, open circuit potential measurements (OCP) of each sample were conducted, and the double-layer capacitance was measured by CV in a potential range of ± 25 mV of the OCP at varying scan rates (10, 20, 40, 60, 80, 100, 150 mV $s^{-1}$) going from low scan rates to high scan rates. From the CVs, the current was extracted in the middle of the potential window measured, and the double-layer capacitance $C_{DL}$ was calculated by determining the slope of the current density in regard to the geometric area as a function of scan rates. The roughness factor was calculated by dividing the $C_{DL}$ of the coated electrode by the $C_{DL}$ of a planar electrode as a reference, assuming that the number of active sites is linearly proportional to the $C_{DL}$. A calculation to determine the roughness factor was previously described in the literature [3,39]. A planar copper electrode was used for copper particles, and a planar CuZn 80/20 electrode was used for CuZn particles.

### 2.8. Product analysis and quantification

Liquid product analysis was performed using an HPLC (Vanquish HPLC, ThermoFisher) with a HyperREZ™ XP carbohydrate-H+ LC-column. Aliquots of 10 µL of each sample was injected into the column. The

eluent used was 5 mM $H_2SO_4$ in water; measurements were conducted with a flow rate of 0.6 mL $min^{-1}$ and a column temperature of 55 °C. The wavelength was set at 210 nm. Oxalic acid calibration was performed using 6 standard solutions (0 mM, 0.2 mM, 0.35 mM, 0.5 mM, 0.65 mM, and 1 mM). Evaluation of the measurements were performed using the Chromeleon software from ThermoFisher.

Measurements for product analysis were performed using a 4 $cm^2$ electrode (Section 3.1) with catalyst material coated on carbon paper. A H-cell with a glass frit separating anode and cathode compartment was used; for gas analysis, it was assured that the lids were gas-tight. The CAs were performed holding a potential of −2 V vs. Ag/AgCl ($KCl_{sat}$ in $H_2O$).

For liquid analysis, the potential was held for 10 h to obtain samples, and the electrolyte was constantly flushed with $CO_2$ to ensure the presence of $CO_2$ during the experiment. After the electrochemical measurement, 1 mL of electrolyte was taken as a sample for analysis. The Faradaic Efficiency was calculated with Eq. 1

$$FE = \frac{F \cdot z \cdot c \cdot V}{Q} \quad (1)$$

With F being the Faradaic constant, $z$ is the number of electrons transferred, $c$ is the concentration of the analyzed product, $V$ is the volume of the electrolyte of the gas phase, and $Q$ is the transferred electric charge.

Gaseous products were analyzed with a GC (GC-2030, Shimadzu). The detector used was a BID, with a temperature set at 250 °C and a gas flow of 50 mL $min^{-1}$ using He as a carrier gas. GC calibration was performed using three different CO concentrations from 0 vol% to 2 vol%. Evaluation of the measurements was performed using Shimadzu's PostRun Analysis Software.

To obtain samples for the analysis of gaseous products, the potential was held for 1 h, and the electrolyte was saturated with $CO_2$ before the measurement and continuously flushed with during the experiment with a $CO_2$ gas flow of 6.84 mL $min^{-1}$. A sample of the gas flow was periodically injected into the GC. The following equation was used for the calculation of the Faradaic Efficiency (Eq. 2).

$$FE = \frac{F \cdot z \cdot c \cdot v \cdot P}{R \cdot T \cdot I} \quad (2)$$

With F being the Faradaic constant, $z$ is the number of electrons transferred, $c$ is the concentration of the analyzed product, $v$ is the $CO_2$ gas flow rate, P is the ambient pressure, T is the Temperature and $I$ is the average current over 100 s before sampling.

The partial current density towards CO was calculated with the following equation (eq. 3).

$$j_{CO} = \frac{i}{A_{ECSA}} \cdot FE_{CO}$$

With $j_{CO}$ as the current density towards CO, $i$ the measured current, $A_{ECSA}$ the electrochemical active surface area (determined as described in chapter 2.7) and $FE_{CO}$ the Faradaic Efficiency towards CO.

### 2.9. XAS measurements

The operando X-ray absorption spectroscopy measurements at Cu-K and Zn-K edge (8979 eV and 9659 eV, respectively) were performed at the CAT-ACT beamline of KIT Light Source (Karlsruhe, Germany)[61]. The incident photon energy is selected via a double crystal monochromator equipped with a Si (111) crystal pair. The experiments were conducted in transmission mode, using ionization chambers before and after the sample and as well as before and after the reference metal foil. The energy calibration was conducted using the reference metal foil recorded with each experimental spectrum. The spectra were energy calibrated and normalized using the ATHENA program from the IFFEFIT software package[62].

A flow cell which was previously reported in a publication by Czioska *et al.* with a peristaltic pump (Ismatec Reglo)[63]. Cu and CuZn 80/20 were coated on Freudenberg H23C2 carbon paper as a working electrode, and platinum was sputtered on Freudenberg H23C2 as a counter electrode. Electrolytes used were 0.1 M $TBABF_4$ in DMF and 0.1 M $TBABF_4$ in MeCN. The pump was set to a flow rate of 200 µL $min^{-1}$. As a reference electrode a Ag/AgCl ($KCl_{sat}$ in $H_2O$) was used. Chronoamperometric measurements (OCV; −0.8 V; −1.2; −1.4 V; −1.6 V; −1.8 V; −2 V; −2.2 V) were performed, and each potential was held for one hour.

## 3. Results and discussion

In the following section, we report on the electrochemical preparation of the Cu and CuZn catalyst materials and their physical characterization. In addition, we identified their electrochemical performances and selectivities in MeCN and DMF-based electrolytes. Lastly, the catalysts state and their stability were studied using operando XAS experiments.

### 3.1. Cu and CuZn nanoparticle catalysts

The freshly synthesized Cu, CuZn and Zn nanoparticles prepared by flame spray pyrolysis (FSP) were obtained as metal oxides. The elemental composition of CuZnO nanoparticles (80/20, 75/25, 50/50, 25/50 were confirmed by ICP-MS measurements. Electrochemical preliminary tests showed no activity of the metal oxides towards $CO_2$RR in organic electrolytes. Therefore, the NPs were electrochemically reduced to their metallic form. The reduction was carried out in 1 M NaOH for Cu and 0.1 M $KHCO_3$ for CuZn and Zn, as dissolution took place under alkaline conditions. The reduction was more efficient in cyclic voltammetry than in chronoamperometry. Optimal results were obtained after preconditioning the catalyst by an oxidation/reduction sequence with three cycles over a wide potential range (1.5 V to −1.5 V vs. RHE in NaOH and 1 V to −1 V vs RHE in $KHCO_3$), followed by cycling below −0.3 to −1.5 V until complete reduction (Fig. 2 and S3).

Complete conversion was verified by XRD, measuring the catalyst particles on the carbon electrode support before and after electrochemical reduction (Fig. 3). The XRD patterns obtained for the as-prepared CuO NPs show broad reflections at 35.5°, 38.7°, 48.7°, 58.2°, 61.5°, 66.1° and 67.8° which corresponds to (1−1−1), (111), (20−2), (202), (1−1−3), (022) and (220) (Fig. 3a)[64]. This is in good agreement with the crystalline planes of CuO in the monoclinic space group C12c1 and JCPDS file no. 892531. Rietveld refinement also shows a 99.9 % agreement with CuO and 0.1 % agreement with $Cu_2O$. The reduced Cu catalyst has peaks at diffraction angles of 43.3°, 50.5°, and 74.2° corresponding to (111), (002), and (022), the characteristic face-centered cubic (fcc) copper with the space group Fm-3m which is in good agreement with JCPDS file no. 892531[65]. In addition to pure copper, a percentage of > 7 % was found for $CuO_x$.

The diffractogram of CuZnO 80/20 NPs is shown in Fig. 3b. The reflections at 2θ of 36.3°, 39.9°, 46.1°, 58.5°, 62.5°, and 78.1° correspond to (111) (011) (002), (200), (1−1−2), (110), (013) and (022) (222) planes. All peaks can be indexed to ZnO (zincite) with the space group P63 mc (JCPDS file no. 00–036–1451), $Cu_2O$ (cuprite) in the cubic Pn-3m space group, and the crystalline planes of copper oxide (CuO) in the monoclinic (tenorite) space group C12/c1. The reduced CuZn 80/20 NPs show a distinct diffraction peak at 2θ = 43.5° diffraction angle corresponding to (111) planes of the CuZn 90/10 with the space group Pn-3m[66]. The CuZn is brass in the α phase (81.5 %), whereas 6.9 % cuprite, 2.1 % ZnO, and 1.6 % Cu remain. Similar observation was made for CuZnO and CuZn (75/25) (Fig. 3c). For CuZnO NPs with a ratio of 50/50 and 25/50, complex mixtures of α-brass, cuprite, ZnO and Cu were found (Fig. S1). The literature shows that alloys with a zinc content below 32.5 % crystallize in the face-centered cubic (cfc) CuZn-α phase, most likely in a ratio of 75/25 [66].

Additional SEM/EDX analysis supports the findings (Fig. S4-S5).

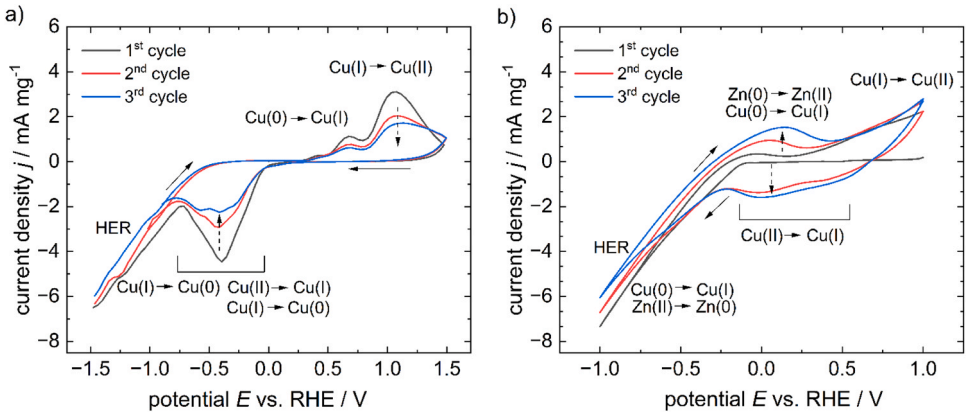


**Fig. 2.** CVs of the first three reduction cycles of a. CuO to Cu in 0.1 M $NaOH_{(aq)}$ and b. CuZnO 80/20 to CuZn 80/20 in 0.1 M $KHCO_{3(aq)}$.

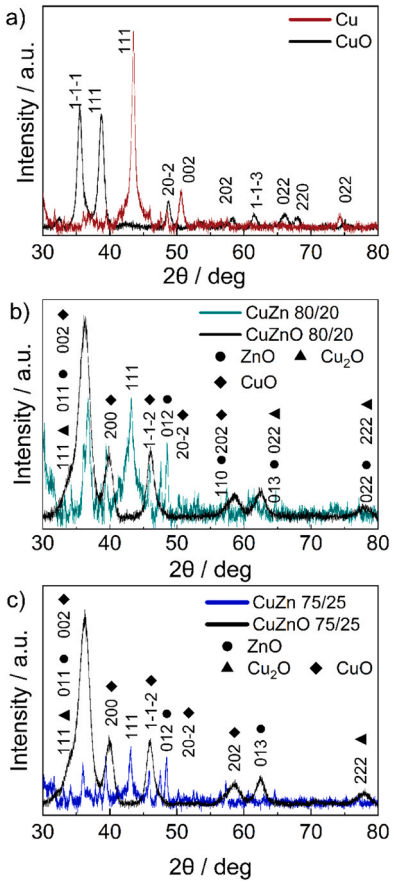


**Fig. 3.** X-ray diffractograms of the materials as prepared from flame spray pyrolysis and after the electrochemical reduction. a) CuO and Cu, b) CuZnO (80/20) and CuZn (80/20), and c) CuZnO (75/25) and CuZn (75/25).

Overall, the catalyst analysis confirms the success of electrochemical reduction. In electrochemical processes such as $CO_2$RR, the size of the catalyst particles is a crucial parameter, as smaller sizes result in a larger surface area and can ultimately reduce the catalyst loading. The mean crystallite sizes were calculated by Rietveld refinement (Table 1). The mean crystallite sizes for CuO and CuZnO NPs are in a similar magnitude $< 20$ nm. During electrochemical reduction, the metallic catalysts double their mean crystallite size, resulting in particle dimensions between 20 and 30 nm. Further results of Rietveld refinement regarding composition of the catalyst materials can be found in the Table S1.

**Table 1**
Mean crystallite sizes of the NP before and after the reduction procedure. XRD was performed with coated catalyst material and Nafion® ionomer on carbon paper. Rietveld refinement was done using TOPAS software.

| Nanoparticle oxides | Mean crystallite size [nm] | Metallic nanoparticles | Mean crystallite size [nm] |
|---|---|---|---|
| CuO | 11.8 | Cu | 21.7 |
| CuZnO 80/20 | 17.5 | CuZn 80/20 | 26.8 |
| CuZnO 75/25 | 12.5 | CuZn 75/25 | 27.4 |
| CuZnO 50/50 | 6.3 | CuZn 50/50 | 12.0 |
| CuZnO 25/75 | 9.9 | CuZn 25/75 | 26.3 |
| ZnO | 29.9 | Zn | 43.1 |

### 3.2. *Performance and selectivity analysis of $CO_2$RR*

Cyclic voltammograms were recorded in a stagnant $CO_2$-saturated 0.1 M tetra-*N*-butylammonium tetrafluoroborate ($TBABF_4$) / DMF electrolyte to evaluate the electrochemical activities of the as prepared metal oxide and in-situ prepared metal catalyst electrodes during $CO_2$RR. All voltammograms of the CuO and CuZnO metal oxides as well as metallic zinc showed marginal activity (see Fig. S2), which highlights the importance of the electrochemical reduction procedure. In contrast, all Cu and CuZn NPs show good activity towards $CO_2$RR (Fig. 4). The CVs for Cu and CuZn 50/50 and 25/75 show similar profiles with indistinguishable features. At −1.5 V vs. Ag/AgCl during the forward sweep, a cathodic current occurs with an exponential trend and no visible limitation. The maximum current densities were 3–4 times lower than for CuZn 80/20 and 75/25, which exhibited the highest activity of all catalysts.

CuZn 80/20 and 75/25 differ majorly, due to their alloyed material composition. Above −1.2 V vs. Ag/AgCl, they show a strong (pseudo-) capacitive behavior. Below −1.2 V, a steep cathodic current with an exponential increase occurs during the forward sweep. The slopes increase at −1.5 or −1.6 V. For CuZn 80/20, it flattens out beyond −1.65 V, suggesting a possible transport limitation. The current density during the backward sweeps for CuZn 80/20 and 75/25 decreases rapidly and then becomes constant without showing any feature.

The overall activity of the catalyst material is an important factor, and the initial potential determines how much electrical energy is required for the reaction to proceed. The initial potentials were determined by evaluating the derivative $dj/dE$ during the forward sweep, where the change in slope in the CV was determined with the initial potential at $dj/dE = 3$ (Fig. 4b). The onset potential at −1.53 V found for the Cu NP is in good agreement with the literature found at −1.5 V for flat copper[67]. The formation of α-brass nanoparticles (Zn content of 20 and 25 wt%) significantly reduces the overvoltage to −1.13 V and −1.2 V vs. Ag/AgCl. Higher Zn content increases the overpotential to

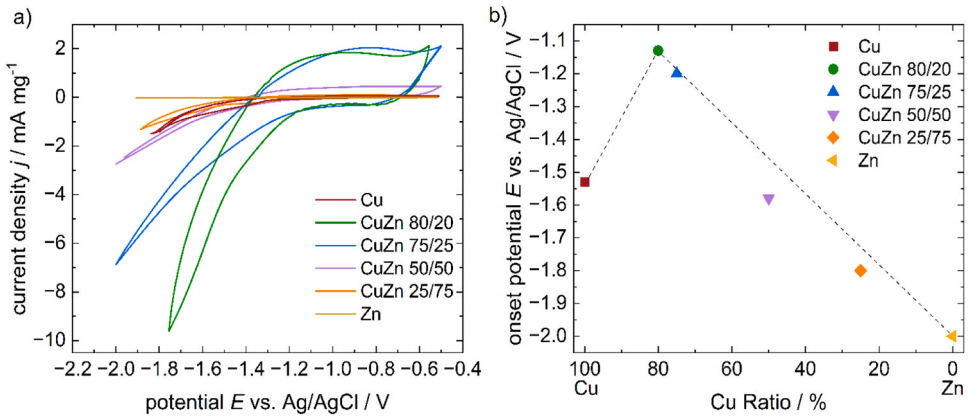


**Fig. 4.** a) CVs for a scan rate of 50 mV $s^{-1}$ for different CuZn ratios in the catalyst material. All CVs were performed in 0.1 M $TBABF_4$ in DMF The iR-corrected third cycle is given vs. Ag/AgCl ($KCl_{sat}$ in $H_2O$). Potential limits are chosen to avoid catalyst or electrolyte degradation. Current density was calculated in mA $mg^{-1}$ in regard to the mass of the coating as the mixed phases of the different CuZn particles did not meet the criteria for $C_{DL}$ analysis. b) Comparison of the onset potentials of the different catalyst materials in $CO_2$RR. The initial potentials were determined by evaluating the change in the forward sweep of the CV; initial potential was determined at dj/dE = 3.

−1.58 V for CuZn 50/50 and −1.8 V for CuZn 25/75. Zn did not meet the criteria of d$j$/d$E$ = 3; the onset was therefore set to −2 V. This indicates that metallic Zn shows no significant activity for $CO_2$ reduction under aprotic conditions (see Fig. S2e and f). This observation is somewhat surprising, as Zn is known to exhibit considerable activity for $CO_2$-to-CO conversion in aqueous electrolytes.

A comprehensive understanding of $CO_2$RR in organic electrolytes requires not only insights into catalyst material properties but also a systematic evaluation of electrolyte effects. To investigate the interplay between catalyst and solvent, we employed two commonly used the aprotic solvents DMF and MeCN each containing 0.1 M $TBABF_4$ as supporting electrolyte. These solvents were selected based on their high $CO_2$ solubility, aprotic nature, and proven electrochemical stability under $CO_2$RR conditions[53]. For performance and product analyses, we selected Cu, CuZn 80/20, and CuZn 75/25 as catalyst materials. These compositions exhibited the highest catalytic activity (see Fig. 4) and showed a homogeneous morphology and phase composition (see Table S1 and Fig. S5), which are essential prerequisites for a reliable and quantitative evaluation of catalytic performance and catalyst state.

For the following analysis, chronoamperometry measurements were performed. The Cu and CuZn catalysts show different behavior in DMF (Fig. 5a). Cu shows one slope of −0.674 V $dec^{-1}$ over the whole potentials range. Both CuZn catalysts show two slopes in DMF based electrolytes. CuZn 80/20 shows the first slope of −0.19 V $dec^{-1}$ in a potential region between −1.4 V and −1.55 V; the second slope below potentials of −1.55 V has a value of −1.345 V $dec^{-1}$. The first slope for CuZn 75/25 is between −1.2 V and −1.5 V and has a value of −0.34 V $dec^{-1}$; the second slope below potentials of −1.5 V has a value of −1.28 V $dec^{-1}$.

All investigated catalyst materials show two slopes in the MeCN-based electrolyte (Fig. 5b). The first slope of Cu starts at a potential of −1.55 V with a value of −0.45 V $dec^{-1}$; a change in slope can be detected at −1.85 V $dec^{-1}$; below this potential, a slope of −0.9 V $dec^{-1}$ can be observed. CuZn 80/20 shows the first slope between −1.4 V and −1.75 V with a value of −0.4 V $dec^{-1}$; the second slope of −1.22 V $dec^{-1}$ is below potentials of −1.75 V. The slopes of CuZn 75/25 are in the same potential regions as CuZn 80/20. The first slope has a value of −0.5 V $dec^{-1}$, below −1.75 V, the slope changes to −0.87 V $dec^{-1}$.

This means alloying copper and zinc and forming brass in the α-phase leads to a significantly lower overpotential than copper or zinc need for $CO_2$ reduction. Adsorption has previously been described as the limiting factor in $CO_2$RR on copper in acetonitrile, with a maximum of 25 % of the catalyst surface being used[38]. So far it is unclear what causes the higher activity at CuZn catalysts. One possible explanation for the observed improvement may that Zn enhances $CO_2$ adsorption on the catalyst surface, which could lower the activation barrier and improve the overall reaction kinetics. Similar effects have been reported in aqueous electrolytes, where the addition of Zn to Cu was shown to improve the binding properties of oxygen-containing species, thereby promoting $CO_2$ adsorption and stabilizing oxygenated intermediates on

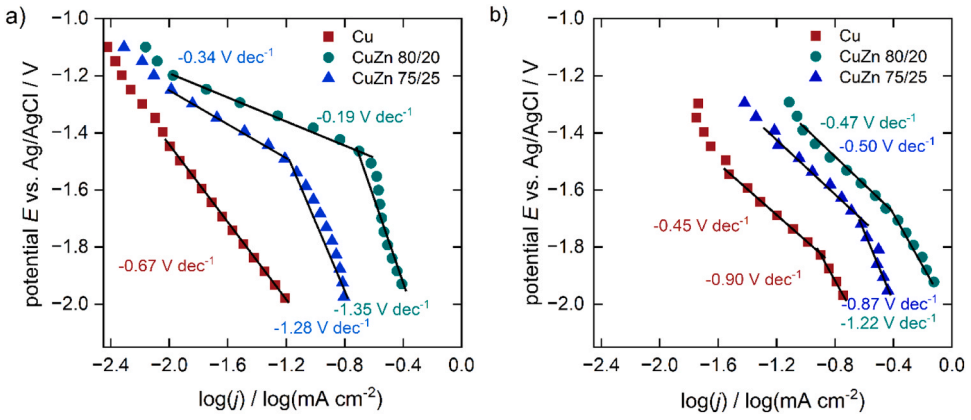


**Fig. 5.** Tafel plots for Cu, CuZn 80/20, and CuZn 75/25 nanoparticles in a) 0.1 M $TBABF_4$ in DMF, b) 0.1 M $TBABF_4$ in MeCN. The potentials are iR-corrected given vs. Ag/AgCl ($KCl_{sat}$ in $H_2O$). Potential limits are chosen to avoid catalyst or electrolyte degradation.

the surface[68]. However, it remains unclear whether this is the definitive cause of the improved performance observed in our system.

The Cu NP in DMF only shows one slope, meaning there is no change in kinetic limitation over the potential range investigated. As previously stated, the addition of zinc to the catalyst material improves the adsorption properties of the catalyst. The different slopes found for the CuZn catalyst in DMF show that the limiting reaction step has changed. Due to the $CO_2$ solubility and the diffusion properties of $CO_2$ in DMF mass transport is possibly the limiting reaction step[54]. In MeCN, all catalyst materials show two different slopes with similar values for the slopes of the different catalysts. As the limiting kinetic step on copper is the $CO_2$ adsorption, the similar slopes of the CuZn 75/25 catalyst indicate an improvement in the adsorption of $CO_2$ but not a complete overcoming of the reaction bottleneck. The last slope (-1.22 V $dec^{-1}$) of CuZn 80/20 in MeCN is similar to both CuZn in DMF which suggests similar kinetic limitation leading to the conclusion that a transport limitation was reached.

Product distribution is an integral part of the evaluation of the catalyst material. In aqueous electrolytes, the selectivity towards valuable products poses a big problem as copper-based catalyst is able to produce different hydrocarbons but with a low selectivity towards the different products. In aprotic organic electrolytes, the number of possible products is limited due to the lack of a proton source, so only CO and oxalate are possible products.

To evaluate the Faradaic efficiency, product analysis was performed by doing chronoamperometry at −2 V vs. Ag/AgCl. Fig. 6 shows the results of the product investigation for Cu, CuZn 80/20, and CuZn 75/25 in 0.1 M $TBABF_4$ in DMF and 0.1 M $TBABF_4$ in MeCN.

CO is the main product for all catalyst material and electrolyte investigated. In DMF, the FE towards CO is 96 % on Cu, 95 % on CuZn 80/20, and 100 % on CuZn 75/25. For copper, the Faradaic efficiency towards oxalate was found to be 0.34 %, in the case of CuZn NP, only traces of oxalate were detected; showing that we were able to gain complete control over the selectivity towards CO. In Acetonitrile, the FE towards CO is between 95 % and 105 % for all catalyst materials. Oxalate was only found, again not enough to do a quantification. The current density $j_{CO}$ towards carbon monoxide is almost four folds higher for CuZn 80/20 than for Cu, emphasizing the influence of the catalyst material on the $CO_2$RR activity.

Our study demonstrates that CuZn (80/20 and 75/25) catalysts significantly enhance performance over Cu by probably by improving $CO_2$ adsorption on the catalyst surface, effectively overcoming the bottleneck in aprotic organic electrolytes. Achieving over 99.9 % FE towards CO in DMF and MeCN-based electrolytes and only traces of oxalate as a product, we gained complete control over the selectivity.

### 3.3. Catalyst state and stability

Information regarding the catalyst state and stability of copper-based catalysts is lacking for the $CO_2$RR in organic electrolytes, whereas it was found that copper undergoes phase changes from $Cu_xO$ to metallic Cu in aqueous electrolytes[12]. The use of aprotic organic electrolytes could lead to a higher bulk stability of the Cu based catalyst materials. In order to investigate possible material changes during the $CO_2$RR in organic electrolytes, X-ray absorption spectroscopy measurements were carried out for CuO, and Cu NP, CuZn 80/20 NP as well as Cu-foil, references used were the Cu foil for metallic Cu, $Cu_2O$ and CuO. The measurements were performed with 0.1 M $TBABF_4$ in DMF and 0.1 M $TBABF_4$ in MeCN. For the measurements, chronoamperometry was conducted, each potential was held for 1 h.

The Cu NP in DMF (Fig. 7a) match well with the Cu foil reference measured showing that the bulk phase is metallic copper. Over the different potentials applied no changes in the course of the curve or the peak position can be detected. A change in intensity is seen which can be

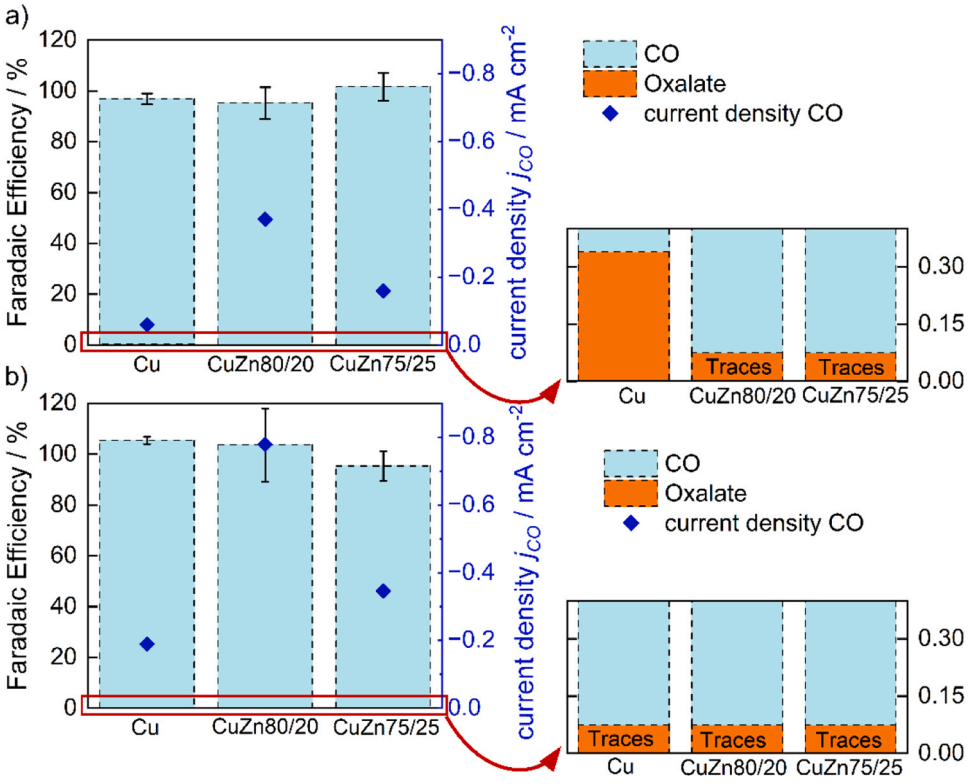


**Fig. 6.** Comparison of the faradaic efficiency and the current density towards CO of the different catalyst materials (Cu, CuZn 80/20 and CuZn 75/25) in a) 0.1 M $TBABF_4$ in DMF, b) 0.1 M $TBABF_4$ in MeCN, measurements were done performing chronoamperometry at −2 V vs. Ag/AgCl ($KCl_{sat}$ in $H_2O$). Karl Fischer Titration showed 200 ppm water content for the electrolyte compositions. The current density towards CO was calculated by detemination of the ECSA, a description of this can be found in chapter 2.7 and 2.8.

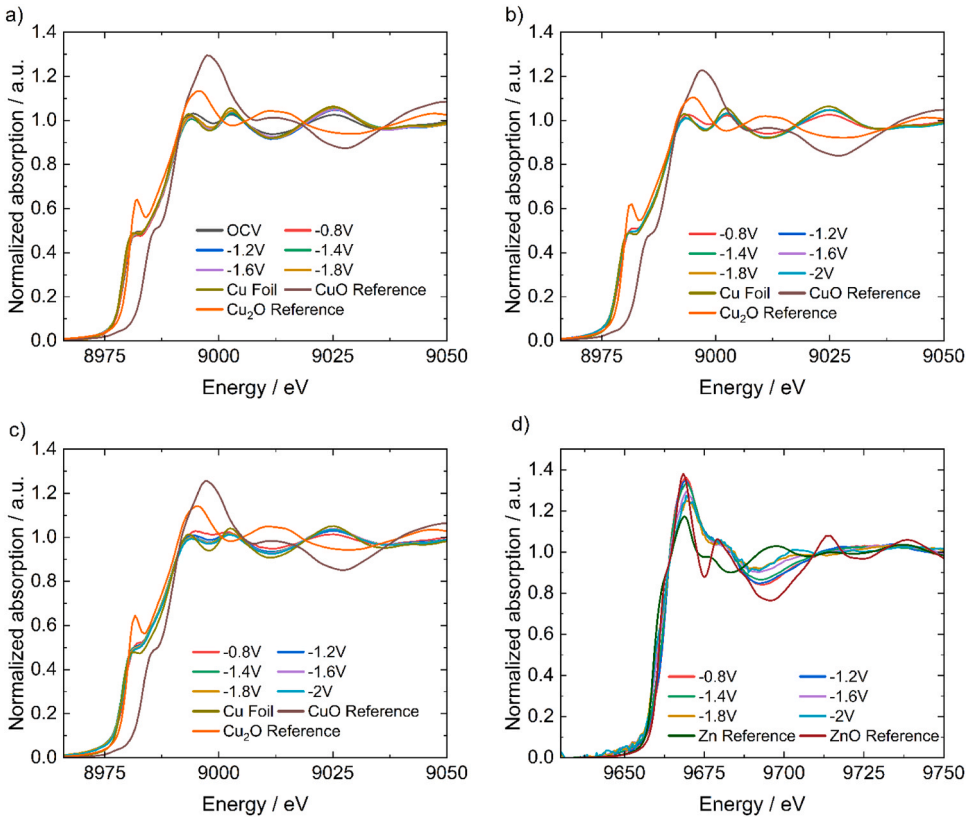


**Fig. 7.** XAS spectra taken during chronoamperometry at different potentials hold for one hour. Spectra shown of a) the Cu K-edge of Cu NP in 0.1 M $TBABF_4$ in DMF; b) Cu K-edge of Cu NP in 0.1 M $TBABF_4$ in MeCN; c) Cu K-edge of CuZn 80/20 NP in 0.1 M $TBABF_4$ in DMF; d) Zn K-edge of CuZn 80/20 in 0.1 M $TBABF_4$ in DMF.

attributed to particle detachment during the experiment due to bubbles in the measurements setup as well as bubbles forming during the experiment. Overall, the particles show a high bulk stability with no phase change within the copper.

The Cu NP in MeCN (Fig. 7b) again matches the Cu foil reference, showing that the bulk phase of the Cu NP is metallic copper. Again, no changes in peak position or curve course are detected, showing that the bulk phase is stable over the different potentials applied. The Cu K-edge of the CuZn 80/20 in DMF (Fig. 7c) shows slight changes in the peak position and peak intensity. The minimum peak at an energy of 8998 eV gains intensity with the step from −0.8 V to −1.2 V. The bulk phase of the copper was not completely reduced at the start of the experiment. With lower potentials than −1.2 V, the curve shows no significant changes, showing again a high bulk stability of the material.

The Zn K-edge of the CuZn 80/20 catalyst (Fig. 7d) matches well with spectra found in literature for brass [69,70], showing that the catalyst is an alloy. At potentials lower than −1.4 V, slight changes in the signal can be seen. The change in whiteline intensity and positions is associated to a change in the alloy [70]. Correlating the changes found in the Cu signal it is possible that some Zn was unalloyed in the bulk phase at the start of the experiment and the small amount of ZnO left in the bulk phase is reduced and alloyed with the copper. Again, the measurement setup and the reaction can lead to bubbles in the system and this can lead to catalyst detachment of the material and therefor to changes in the signal intensity.

The spectra of Cu foil in MeCN and DMF are displayed in S9a and S9b. In both electrolytes, no changes were seen for the copper foil, meaning that it is stable under the reaction conditions applied.

Spectra of CuO NP in DMF (Fig. S9c) match with the CuO reference taken confirming results found in the XRD analysis. Over the different potentials, changes in peak intensity are detected at peaks at energies of 8997 eV and 9026 eV. This shows that CuO is not bulk stable and phase changes are happening. The CuO NP in MeCN (Fig. S9d) show no changes in signal.

With this we were able to show that the bulk of our catalyst material is Cu and Zn which act as the active species for the $CO_2$RR. Cu and CuZn have shown a high long-term bulk stability over a potential range of −0.8 V up to −2 V vs. Ag/AgCl. Additionally, chronoamperometric stability measurements over a duration of 100 h are shown in Fig. S10, showing longterm stability in the electrochemical measurements.

## 4. Conclusion

In this study, we have investigated the synthesis, performance and stability of Cu and CuZn nanoparticle catalysts for the $CO_2$ reduction reaction in DMF and acetonitrile electrolytes. The catalysts were prepared as metal oxides via flame spray pyrolysis and then reduced to their metallic forms using cyclic voltammetry and chronoamperometry. X-ray diffraction and Rietveld refinement confirmed the successful conversion of Cu and CuZn oxides into metallic nanoparticles with crystallite sizes of 20–30 nm after reduction.

Electrochemical testing indicated that although the metal oxides showed little activity for $CO_2$RR, the reduced Cu and CuZn catalysts showed significantly improved performance. Among the catalysts, the CuZn alloys, especially with compositions of 80/20 and 75/25, showed the highest activity and selectivity towards CO, with a Faradaic efficiency of over 95 % in both organic electrolytes. These compositions also showed significantly lower overpotentials compared to pure copper, which highlights the positive effect of alloying zinc with copper in improving $CO_2$ adsorption and reducing the activation barrier.

Furthermore, our study investigated the long-term stability of the catalysts using operando X-ray absorption spectroscopy. The bulk stability of Cu and CuZn catalysts was confirmed over a wide potential range, with no significant phase changes observed, indicating their

robustness during prolonged operations. The stability of α-brass phase in CuZn catalysts was particularly noteworthy, with no significant degradation observed, ensuring catalyst longevity during $CO_2$RR.

Overall, this work highlights the potential of CuZn alloy catalysts, particularly in the 80/20 and 75/25 compositions, for efficient and selective $CO_2$ reduction in organic electrolytes. The improved $CO_2$ electrochemical properties and long-term stability make these materials promising candidates for further development in $CO_2$ electroreduction applications in non-aqueous electrolytes, and may serve as a basis for optimizing system parameter for $CO_2$RR, e.g. electrolyte and catalyst composition.

## CRediT authorship contribution statement

**Steffen Czioska:** Methodology, Investigation. **Enrico Tusini:** Formal analysis. **Leonie Wildersinn:** Methodology, Investigation, Formal analysis. **Ruth Witzel:** Writing – original draft, Investigation, Formal analysis, Data curation. **Philipp Röse:** Writing – review & editing, Supervision, Resources, Project administration, Methodology, Conceptualization. **Jan-Dierk Grunwaldt:** Writing – review & editing, Supervision. **Anna Zimina:** Writing – review & editing, Supervision, Conceptualization. **Inga Dorner:** Writing – review & editing, Methodology, Investigation.

## Declaration of Competing Interest

The authors declare that they have no known competing financial interests or personal relationships that could have appeared to influence the work reported in this paper.

## Acknowledgments

We sincerely thank Lorena Baumgarten, associated with the Institute for Chemical Technology and Polymer Chemistry (ITCP) at the Karlsruhe Institute of Technology for preparation of the catalyst materials used in this study. We also sincerely acknowledge Annette Schucker, associated with the Institute for Applied Materials – Electrochemical Technologies at the Karlsruhe Institute of Technology for the SEM/EDX measurements. We thank Claudia Mößner for performing ICP-MS analysis. We would like to thank the Institute for Beam Physics and Technology (IBPT) for the operation of the storage ring, the Karlsruhe Research Accelerator (KARA). We acknowledge the KIT Light Source for provision of instruments at the CAT-ACT beamline of the Institute of Catalysis Research and Technology (IKFT), in particular Dr. Danielle Santos Goncalves (IKFT) for her help and technical support during experiments.

## Appendix A. Supporting information

Supplementary data associated with this article can be found in the online version at doi:10.1016/j.jcou.2025.103138.

## Data availability

The data presented in the manuscript are openly available in the KITopen repository at: DOI 10.35097/yHRzUdfUUFDRzWDr.

## References

[1] C. Graves, S.D. Ebbesen, M. Mogensen, K.S. Lackner, Sustainable hydrocarbon fuels by recycling $CO_2$ and $H_2O$ with renewable or nuclear energy, Ren. Sustain. Energy Rev. 15 (2011) 1–23, https://doi.org/10.1016/j.rser.2010.07.014.

[2] Y. Jia, F. Li, K. Fan, L. Sun, Cu-based bimetallic electrocatalysts for $CO_2$ reduction, APM 1 (2022) 100012, https://doi.org/10.1016/j.apmate.2021.10.003.

[3] A.H.M. Da Silva, S.J. Raaijman, C.S. Santana, J.M. Assaf, J.F. Gomes, M.T. M. Koper, Electrocatalytic $CO_2$ reduction to $C_2$+ products on Cu and $Cu_xZn_y$ electrodes: Effects of chemical composition and surface morphology, J. Electroanal. Chem. 880 (2021) 114750, https://doi.org/10.1016/j.jelechem.2020.114750.

[4] S. Van Daele, L. Hintjens, J. Van den Hoek, S. Neukermans, N. Daems, J. Hereijgers, T. Breugelmans, Influence of the target product on the electrochemical reduction of diluted $CO_2$ in a continuous flow cell, J. $CO_2$ Util. 65 (2022) 102210, https://doi.org/10.1016/j.jcou.2022.102210.

[5] G. Marcandalli, M.C.O. Monteiro, A. Goyal, M.T.M. Koper, Electrolyte Effects on $CO_2$ Electrochemical Reduction to CO, Acc. Chem. Res. 55 (2022) 1900–1911, https://doi.org/10.1021/acs.accounts.2c00080.

[6] C.D. Koolen, J.K. Pedersen, B. Zijlstra, M. Winzely, J. Zhang, T.V. Pfeiffer, W. Vrijburg, M. Li, A. Agarwal, Z. Akbari, Y. Kuddusi, J. Herranz, O.V. Safonova, A. Schmidt-Ott, W. Luo, A. Zuettel, Scalable synthesis of Cu-cluster catalysts via spark ablation for the electrochemical conversion of $CO_2$ to acetaldehyde, Nat. Synth. 4 (2025) 336–346, https://doi.org/10.1038/s44160-024-00705-3.

[7] S. Nitopi, E. Bertheussen, S.B. Scott, X. Liu, A.K. Engstfeld, S. Horch, B. Seger, I.E. L. Stephens, K. Chan, C. Hahn, J.K. Nørskov, T.F. Jaramillo, I. Chorkendorff, Progress and Perspectives of Electrochemical $CO_2$ Reduction on Copper in Aqueous Electrolyte, Chem. Rev. 119 (2019) 7610–7672, https://doi.org/10.1021/acs.chemrev.8b00705.

[8] A. Bagger, O. Christensen, V. Ivaništšev, J. Rossmeisl, Catalytic $CO_2$ /CO Reduction: Gas, Aqueous, and Aprotic Phases, ACS Catal. 12 (2022) 2561–2568, https://doi.org/10.1021/acscatal.1c05358.

[9] Y.Y. Birdja, E. Pérez-Gallent, M.C. Figueiredo, A.J. Göttle, F. Calle-Vallejo, M.T. M. Koper, Advances and challenges in understanding the electrocatalytic conversion of carbon dioxide to fuels, Nat. Energy 4 (2019) 732–745, https://doi.org/10.1038/s41560-019-0450-y.

[10] I.E.L. Stephens, K. Chan, A. Bagger, S.W. Boettcher, J. Bonin, E. Boutin, A. K. Buckley, R. Buonsanti, E.R. Cave, X. Chang, S.W. Chee, A.H.M. da Silva, P. de Luna, O. Einsle, B. Endrődi, M. Escudero-Escribano, J.V.F. de Araujo, M. C. Figueiredo, C. Hahn, K.U. Hansen, S. Haussener, S. Hunegnaw, Z. Huo, Y. J. Hwang, C. Janáky, B.S. Jayathilake, F. Jiao, Z.P. Jovanov, P. Karimi, M.T. M. Koper, K.P. Kuhl, W.H. Lee, Z. Liang, X. Liu, S. Ma, M. Ma, H.-S. Oh, M. Robert, B.R. Cuenya, J. Rossmeisl, C. Roy, M.P. Ryan, E.H. Sargent, P. Sebastián-Pascual, B. Seger, L. Steier, P. Strasser, A.S. Varela, R.E. Vos, X. Wang, B. Xu, H. Yadegari, Y. Zhou, 2022 roadmap on low temperature electrochemical $CO_2$ reduction, J. Phys. Energy 4 (2022) 042003, https://doi.org/10.1088/2515-7655/ac7823.

[11] P. Grosse, A. Yoon, C. Rettenmaier, A. Herzog, S.W. Chee, B. Roldan Cuenya, Dynamic transformation of cubic copper catalysts during $CO_2$ electroreduction and its impact on catalytic selectivity, Nat. Commun. 12 (2021) 6736, https://doi.org/10.1038/s41467-021-26743-5.

[12] X. Wang, K. Klingan, M. Klingenhof, T. Möller, J. Ferreira de Araújo, I. Martens, A. Bagger, S. Jiang, J. Rossmeisl, H. Dau, P. Strasser, Morphology and mechanism of highly selective Cu(II) oxide nanosheet catalysts for carbon dioxide electroreduction, Nat. Commun. 12 (2021) 794, https://doi.org/10.1038/s41467-021-20961-7.

[13] M. Fields, X. Hong, J.K. Nørskov, K. Chan, Role of Subsurface Oxygen on Cu Surfaces for $CO_2$ Electrochemical Reduction, J. Phys. Chem. C 122 (2018) 16209–16215, https://doi.org/10.1021/acs.jpcc.8b04983.

[14] S.J. Raaijman, N. Arulmozhi, M.T.M. Koper, Morphological Stability of Copper Surfaces under Reducing Conditions, ACS Appl. Mater. Interfaces 13 (2021) 48730–48744, https://doi.org/10.1021/acsami.1c13989.

[15] J. Yu, Y. Zheng, B. Lv, A. Huang, J. Zhang, Z. Wang, Y. Zhang, Y. Wu, Y. Zhou, Y. Wang, W. Luo, Structural transformation of copper-coordinated COFs drives enhanced multi-carbon selectivity in $CO_2$ electroreduction, Appl. Cat. B Environ. Energy 368 (2025) 125131, https://doi.org/10.1016/j.apcatb.2025.125131.

[16] A. Goyal, G. Marcandalli, V.A. Mints, M.T.M. Koper, Competition between $CO_2$ Reduction and Hydrogen Evolution on a Gold Electrode under Well-Defined Mass Transport Conditions, J. Am. Chem. Soc. 142 (2020) 4154–4161, https://doi.org/10.1021/jacs.9b10061.

[17] B. Lv, J. Yu, F. Zhou, Z. Wang, J. Zhang, Y. Zhang, Y. Wu, Y. Wang, W. Luo, Unraveling the enhanced urea selectivity in electroreduction of CO2 and nitrate over Bimetallic CuZn catalysts, Mol. Cat. 578 (2025) 114978, https://doi.org/10.1016/j.mcat.2025.114978.

[18] B.J.M. Etzold, U. Krewer, S. Thiele, A. Dreizler, E. Klemm, T. Turek, Understanding the activity transport nexus in water and $CO_2$ electrolysis: state of the art, challenges and perspectives, Chem. Eng. J. 424 (2021) 130501, https://doi.org/10.1016/j.cej.2021.130501.

[19] I. Dorner, P. Röse, U. Krewer, Dynamic vs. Stationary Analysis of Electrochemical Carbon Dioxide Reduction: Profound Differences in Local States, ChemElectroChem 10 (2023) e202300387, https://doi.org/10.1002/celc.202300387.

[20] H. Ooka, M.C. Figueiredo, M.T.M. Koper, Competition between Hydrogen Evolution and Carbon Dioxide Reduction on Copper Electrodes in Mildly Acidic Media, Langmuir 33 (2017) 9307–9313, https://doi.org/10.1021/acs.langmuir.7b00696.

[21] A. Bagger, W. Ju, A.S. Varela, P. Strasser, J. Rossmeisl, Single site porphyrine-like structures advantages over metals for selective electrochemical $CO_2$ reduction, Catal. Today 288 (2017) 74–78, https://doi.org/10.1016/j.cattod.2017.02.028.

[22] C. Amatore, J.M. Saveant, Mechanism and kinetic characteristics of the electrochemical reduction of carbon dioxide in media of low proton availability, J. Am. Chem. Soc. 103 (1981) 5021–5023, https://doi.org/10.1021/ja00407a008.

[23] E. Lamy, L. Nadjo, J.M. Saveant, Standard potential and kinetic parameters of the electrochemical reduction of carbon dioxide in dimethylformamide, J. Electroanal. Chem. Interf. Electrochem. 78 (1977) 403–407, https://doi.org/10.1016/S0022-0728(77)80143-5.

[24] A. Gennaro, A.A. Isse, E. Vianello, Solubility and electrochemical determination of $CO_2$ in some dipolar aprotic solvents, J. Electroanal. Chem. Interf. Electrochem 289 (1990) 203–215, https://doi.org/10.1016/0022-0728(90)87217-8.

[25] C.M. Hansen. Hansen Solubility Parameters: A User's Handbook, second ed., CRC Press, 2007 https://doi.org/10.1016/j.isci.2019.07.014.
[26] S. Garg, M. Li, A.Z. Weber, L. Ge, L. Li, V. Rudolph, G. Wang, T.E. Rufford, Advances and challenges in electrochemical $CO_2$ reduction processes: an engineering and design perspective looking beyond new catalyst materials, J. Mater. Chem. A 8 (2020) 1511–1544, https://doi.org/10.1039/C9TA13298H.
[27] M. König, J. Vaes, E. Klemm, D. Pant, Solvents and supporting electrolytes in the electrocatalytic reduction of $CO_2$, iScience 19 (2019) 135–160, https://doi.org/10.1016/j.isci.2019.07.014.
[28] Y. Matsubara, D.C. Grills, Y. Kuwahara, Thermodynamic aspects of electrocatalytic $CO_2$ reduction in acetonitrile and with an ionic liquid as solvent or electrolyte, ACS Catal. 5 (2015) 6440–6452, https://doi.org/10.1021/acscatal.5b00656.
[29] K. Ito, S. Ikeda, T. Iida, A. Nomura, Electrochemical reduction of carbon dioxide dissolved under high pressure III. In nonaqueous electrolytes, Denki Kagaku Oyobi Kogyo Butsuri Kagaku 50 (1982) 463–469, https://doi.org/10.5796/kogyobutsurikagaku.50.463.
[30] K. Ito, S. Ikeda, N. Yamauchi, T. Iida, T. Takagi, Electrochemical reduction products of carbon dioxide at some metallic electrodes in nonaqueous electrolytes, Bull. Chem. Soc. Jpn. 58 (1985) 3027–3028, https://doi.org/10.1246/bcsj.58.3027.
[31] S. Ikeda, T. Takagi, K. Ito, Selective Formation of Formic Acid, Oxalic Acid, and Carbon Monoxide by Electrochemical Reduction of Carbon Dioxide, Bull. Chem. Soc. Jpn. 60 (1987) 2517–2522, https://doi.org/10.1246/bcsj.60.2517.
[32] T.C. Berto, L. Zhang, R.J. Hamers, J.F. Berry, Electrolyte Dependence of $CO_2$ Electroreduction: Tetraalkylammonium Ions Are Not Electrocatalysts, ACS Catal. 5 (2015) 703–707, https://doi.org/10.1021/cs501641z.
[33] Y. Tomita, S. Teruya, O. Koga, Y. Hori, Electrochemical Reduction of Carbon Dioxide at a Platinum Electrode in Acetonitrile-Water Mixtures, Electrochem. Soc. 147 (2000) 4164, https://doi.org/10.1149/1.1394035.
[34] A.V. Rudnev, M.R. Ehrenburg, E.B. Molodkina, I.G. Botriakova, A.I. Danilov, T. Wandlowski, $CO_2$ Electroreduction on Cu-Modified Platinum Single Crystal Electrodes in Aprotic Media, Electrocatalysis 6 (2015) 42–50, https://doi.org/10.1007/s12678-014-0217-y.
[35] S. Piontek, K. junge Puring, D. Siegmund, M. Smialkowski, I. Sinev, D. Tetzlaff, B. R. Cuenya, U.-P. Apfel, Bio-inspired design: bulk iron–nickel sulfide allows for efficient solvent-dependent $CO_2$ reduction, Chem. Sci. 10 (2019) 1075–1081, https://doi.org/10.1039/C8SC03555E.
[36] M. König, S.-H. Lin, J. Vaes, D. Pant, E. Klemm, Integration of aprotic $CO_2$ reduction to oxalate at a Pb catalyst into a GDE flow cell configuration, Faraday Discuss. 230 (2021) 360–374, https://doi.org/10.1039/D0FD00141D.
[37] R. Gomes, C. Birch, M. Cencer, C. Li, S.-B. Son, I. Bloom, R. Assary, C. Amanchukwu, Probing electrolyte influence on $CO_2$ reduction in aprotic solvents, J. Phys. Chem. C 32 (2022) 13595–13606, https://doi.org/10.26434/chemrxiv-2021-17zmv.
[38] N. Oppel, P. Röse, S. Heuser, M. Prokein, U.-P. Apfel, U. Krewer, Unveiling the kinetics of $CO_2$ reduction in aprotic electrolyte: the critical role of adsorption, Electrochim. Acta 490 (2024) 144270, https://doi.org/10.1016/j.electacta.2024.144270.
[39] B.A. Rohr, A.R. Singh, J.A. Gauthier, M.J. Statt, J.K. Nørskov, Micro-kinetic model of electrochemical carbon dioxide reduction over platinum in non-aqueous solvents, Phys. Chem. Chem. Phys. 22 (2020) 9040–9045, https://doi.org/10.1039/C9CP05751J.
[40] V. Boor, J.E.B.M. Frijns, E. Perez-Gallent, E. Giling, A.T. Laitinen, E.L.V. Goetheer, L.J.P. van den Broeke, R. Kortlever, W. Jong, O.A. Moultos, T.J.H. Vlugt, M. Ramdin, Electrochemical reduction of $CO_2$ to oxalic acid: experiments, process modeling, and economics, Ind. Eng. Chem. Res. 61 (2022) 14837–14846, https://doi.org/10.1021/acs.iecr.2c02647.
[41] M. Ramdin, B. De Mot, A.R.T. Morrison, T. Breugelmans, L.J.P. van den Broeke, J. P.M. Trusler, R. Kortlever, W. de Jong, O.A. Moultos, P. Xiao, P.A. Webley, T.J. H. Vlugt, Electroreduction of $CO_2$/CO to $C_2$ products: process modeling, downstream separation, system integration, and economic analysis, Ind. Eng. Chem. Res. 60 (2021) 17862–17880, https://doi.org/10.1021/acs.iecr.1c03592.
[42] U. Kaiser, E. Heitz, Zum Mechanismus der elektrochemischen Dimerisierung von $CO_2$ zu Oxalsäure, Ber. der Bunsenges. F. üR. Phys. Chem. 77 (1973) 818–823, https://doi.org/10.1002/bbpc.19730771018.
[43] K. Izutsu. Electrochemistry in Nonaqueous Solutions, 2nd ed., Wiley-VCH, Weinheim, 2009.
[44] E.A. dos Reis, G.T.S.T. da Silva, E.I. Santiago, C. Ribeiro, Revisiting electrocatalytic $CO_2$ reduction in nonaqueous media: promoting $CO_2$ recycling in organic molecules by controlling $H_2$ evolution, Energy Technol. 11 (2023) 2201367, https://doi.org/10.1002/ente.202201367.
[45] T. Jaster, A. Gawel, D. Siegmund, J. Holzmann, H. Lohmann, E. Klemm, U.-P. Apfel, Electrochemical $CO_2$ reduction toward multicarbon alcohols - the microscopic world of catalysts & process conditions, iScience 25 (2022) 104010, https://doi.org/10.1016/j.isci.2022.104010.
[46] C. Deacon-Price, A.H.M. da Silva, C.S. Santana, M.T.M. Koper, A.C. Garcia, Solvent effect on electrochemical $CO_2$ reduction reaction on nanostructured copper electrodes, J. Phys. Chem. C 127 (2023) 14518–14527, https://doi.org/10.1021/acs.jpcc.3c03257.
[47] M.C. Figueiredo, I. Ledezma-Yanez, M.T.M. Koper, In situ spectroscopic study of $CO_2$ electroreduction at copper electrodes in acetonitrile, ACS Catal. 6 (2016) 2382–2392, https://doi.org/10.1021/acscatal.5b02543.
[48] D. Bagchi, M. Riyaz, N. Dutta, G. Chawla, S. R Churipard, A. Kumar Singh, S. C Peter, Operando Investigation of the Origin of C—C Coupling in Electrochemical $CO_2$ Reduction Upon Releasing Bonding Strength, Structural Ordering in Pd—Cu Catalyst, Adv. Energy Mater. 14 (2024) 2402237, https://doi.org/10.1002/aenm.202402237.
[49] Y. Guo, Y. Luo, H. Wang, X. Chen, X. Liu, B. Guo, J. Sun, R. Wang, W. Li, C. Zhao, Mediating Zn loading on Cu-Zn bimetallic catalyst for electrochemical $CO_2$ reduction into tunable syngas, Fuel 392 (2025) 134821, https://doi.org/10.1016/j.fuel.2025.134821.
[50] M. van der Veer, N. Daems, P. Cool, T. Breugelmans, Enhancing selectivity and stability in electrochemical $CO_2$ reduction using tailored sputtered CuAg electrodes, Green. Chem. (2025), https://doi.org/10.1039/D4GC06164K.
[51] N.E. Mendieta-Reyes, A.K. Díaz-García, R. Gómez, Simultaneous electrocatalytic $CO_2$ reduction and enhanced electrochromic effect at $WO_3$ nanostructured electrodes in acetonitrile, ACS Catal. 8 (2018) 1903–1912, https://doi.org/10.1021/acscatal.7b03047.
[52] L.V. Haynes, D.T. Sawyer, Electrochemistry of carbon dioxide in dimethyl sulfoxide at gold and mercury electrodes, Anal. Chem. 39 (1967) 332–338, https://doi.org/10.1021/ac60247a013.
[53] J. Shi, F. Shen, F. Shi, N. Song, Y.-J. Jia, Y.-Q. Hu, Q.-Y. Li, J. Liu, T.-Y. Chen, Y.-N. Dai, Electrochemical reduction of $CO_2$ into CO in tetrabutylammonium perchlorate/propylene carbonate: water effects and mechanism, Electrochim. Acta 240 (2017) 114–121, https://doi.org/10.1016/j.electacta.2017.04.065.
[54] M. König, J. Vaes, D. Pant, E. Klemm, Effect of Solvents on Aprotic $CO_2$ Reduction: A Study on the Role of $CO_2$ Mass Transport in the Product Selectivity between Oxalate and Carbon Monoxide, J. Phys. Chem. C. 127 (2023) 18159–18166, https://doi.org/10.1021/acs.jpcc.3c03992.
[55] D. Niu, H. Wang, H. Li, X. Zhang, The effect of the alkyl chain length of the tetraalkylammonium cation on $CO_2$ electroreduction in an aprotic medium, Electrochem. Commun. 52 (2015) 58–62, https://doi.org/10.1016/j.elecom.2015.01.022.
[56] J.-M. McGregor, J.T. Bender, A.S. Petersen, L. Cañada, J. Rossmeisl, J. F. Brennecke, J. Resasco, Organic electrolyte cations promote non-aqueous CO2 reduction by mediating interfacial electric fields, Nat. Catal. 8 (2025) 79–91, https://doi.org/10.1038/s41929-024-01278-2.
[57] W.Y. Teoh, R. Amal, L. Mädler, Flame spray pyrolysis: An enabling technology for nanoparticles design and fabrication, Nanoscale 2 (2010) 1324–1347, https://doi.org/10.1039/C0NR00017E.
[58] R. Ahmad, M. Hellinger, M. Buchholz, H. Sezen, L. Gharnati, C. Wöll, J. Sauer, M. Döring, J.-D. Grunwaldt, U. Arnold, Flame-made $Cu/ZnO/Al_2O_3$ catalyst for dimethyl ether production, Catal. Commun. 43 (2014) 52–56, https://doi.org/10.1016/j.catcom.2013.08.020.
[59] D. Escalera-López, S. Czioska, J. Geppert, A. Boubnov, P. Röse, E. Saraçi, U. Krewer, J.-D. Grunwaldt, S. Cherevko, Phase- and Surface Composition-Dependent Electrochemical Stability of Ir-Ru Nanoparticles during Oxygen Evolution Reaction, ACS Catal. 11 (2021) 9300–9316, https://doi.org/10.1021/acscatal.1c01682.
[60] J. Geppert, P. Röse, S. Czioska, D. Escalera-López, A. Boubnov, E. Saraçi, S. Cherevko, J.-D. Grunwaldt, U. Krewer, Microkinetic Analysis of the Oxygen Evolution Performance at Different Stages of Iridium Oxide Degradation, J. Am. Chem. Soc. 144 (2022) 13205–13217, https://doi.org/10.1021/jacs.2c03561.
[61] A. Zimina, K. Dardenne, M.A. Denecke, D.E. Doronkin, E. Huttel, H. Lichtenberg, S. Mangold, T. Pruessmann, J. Rothe, T. Spangenberg, R. Steininger, T. Vitova, H. Geckeis, J.-D. Grunwaldt, CAT-ACT-A new highly versatile x-ray spectroscopy beamline for catalysis and radionuclide science at the KIT synchrotron light facility ANKA, Rev. Sci. Instrum. 88 (2017) 113113, https://doi.org/10.1063/1.4999928.
[62] B. Ravel, M. Newville, ATHENA, ARTEMIS, HEPHAESTUS: data analysis for X-ray absorption spectroscopy using IFEFFIT, J. Synchrotron Radiat. 12 (2005) 537–541, https://doi.org/10.1107/S0909049505012719.
[63] S. Czioska, K. Ehelebe, J. Geppert, D. Escalera-López, A. Boubnov, E. Saraçi, B. Mayerhöfer, U. Krewer, S. Cherevko, J.-D. Grunwaldt, Heating up the OER: Investigation of $IrO_2$ OER Catalysts as Function of Potential and Temperature, ChemElectroChem 9 (2022) e202200514, https://doi.org/10.1002/celc.202200514.
[64] S. Suresh, S. Karthikeyan, K. Jayamoorthy, FTIR and multivariate analysis to study the effect of bulk and nano copper oxide on peanut plant leaves, J. Sci.: Adv. Mat. Dev. 1 (2016) 343–350, https://doi.org/10.1016/j.jsamd.2016.08.004.
[65] M. Raffi, S. Mehrwan, T.M. Bhatti, J.I. Akhter, A. Hameed, W. Yawar, M.M. ul Hasan, Investigations into the antibacterial behavior of copper nanoparticles against Escherichia coli, Ann. Microbiol 60 (2010) 75–80, https://doi.org/10.1007/s13213-010-0015-6.
[66] V.J. Keast, J. Ewald, K.S.B. De Silva, M.B. Cortie, B. Monnier, D. Cuskelly, E.H. Kisi, Optical properties and electronic structure of the Cu–Zn brasses, J. Alloy. Compd. 647 (2015) 129–135, https://doi.org/10.1016/j.jallcom.2015.06.136.
[67] A.S. Kumar, M. Pupo, K.V. Petrov, M. Ramdin, J.R. Van Ommen, W. De Jong, R. Kortlever, A Quantitative Analysis of Electrochemical $CO_2$ Reduction on Copper in Organic Amide and Nitrile-Based Electrolytes, J. Phys. Chem. C. 127 (2023) 12857–12866, https://doi.org/10.1021/acs.jpcc.3c01955.
[68] F. Studt, M. Behrens, E.L. Kunkes, N. Thomas, S. Zander, A. Tarasov, J. Schumann, E. Frei, J.B. Varley, F. Abild-Pedersen, J.K. Nørskov, R. Schlögl, The Mechanism of CO and $CO_2$ Hydrogenation to Methanol over Cu-Based Catalysts, ChemCatChem 7 (2015) 1105–1111, https://doi.org/10.1002/cctc.201500123.
[69] H.S. Jeon, J. Timoshenko, F. Scholten, I. Sinev, A. Herzog, F.T. Haase, B. Roldan Cuenya, Operando Insight into the Correlation between the Structure and Composition of CuZn Nanoparticles and Their Selectivity for the Electrochemical $CO_2$ Reduction, J. Am. Chem. Soc. 141 (2019) 19879–19887, https://doi.org/10.1021/jacs.9b10709.
[70] M. Rüscher, A. Herzog, J. Timoshenko, H.S. Jeon, W. Frandsen, S. Kühl, B. R. Cuenya, Tracking heterogeneous structural motifs and the redox behaviour of

copper–zinc nanocatalysts for the electrocatalytic $CO_2$ reduction using operando time resolved spectroscopy and machine learning, Catal. Sci. Technol. 12 (2022) 3028–3043, https://doi.org/10.1039/D2CY00227B.